

Ion counting and temperature determination of Coulomb-crystallized laser-cooled ions in traps using convolutional neural networks

Yanning Yin* and Stefan Willitsch

Department of Chemistry, University of Basel, Klingelbergstrasse 80, 4056 Basel

(Dated: February 26, 2025)

Coulomb crystals, ordered structures of cold ions confined in ion traps, find applications in a variety of research fields. The number and temperature of the ions forming the Coulomb crystals are two key attributes of interest in many trapped-ion experiments. Here, we present a fast and accurate approach of determining these attributes from fluorescence images of the ions based on convolutional neural networks (CNNs). In this approach, we first generate a large number of images of Coulomb crystals with different ion numbers and temperatures using molecular-dynamics simulations and then train CNN models on these images to classify the desired attributes. The classification performance of several common pre-trained CNN models was compared in example tasks. We find that for crystals with ion numbers in the range 100–299 and secular temperatures of 5–15 mK, the best-performing model can discern number variations on the level of one ion with an accuracy of 93% and temperature variations by 1 mK with an accuracy of 92%. Since the trained model can be directly integrated into experiments, in-situ determination of these attributes can be realized in a non-invasive fashion, which has the potential to greatly facilitate the analysis and control of trapped ions in real time.

I. INTRODUCTION

Coulomb crystals, referring to the ordered structures of cold ions confined in ion traps, are an unusual form of matter that has been employed in a variety of research fields including quantum information and computation [1–4], atomic clocks [5], fundamental physics studies [6] and cold and controlled chemistry[7]. Coulomb crystals can be generated by loading ions into radiofrequency (RF) or Penning traps [8] and cooling their motion to millikelvin or even lower temperatures using laser cooling (for suitable atomic ions) or sympathetic cooling (for atomic species that cannot be laser cooled and molecular ions). Since the ions are confined in deep traps in ultrahigh-vacuum chambers where collisions with gas and other perturbations from the surroundings are suppressed, Coulomb crystals can exhibit remarkable stability with lifetimes ranging from minutes to days, allowing the observation, addressing, and manipulation of the ions localized in the trap down to single particle level.

For a Coulomb crystal, the ion number (N) and temperature (T) are two important attributes that are of interest in many experiments. For example, in studies of cold collisions between ions and other species, these two parameters and their variations can provide important information about the collision or reaction process in terms of collision energy and reaction rate [9]. During the past years, different methods have been developed to determine N and T of ions in Coulomb crystals. While N is often obtained by counting ions with fluorescence imaging [10] and time-of-flight mass spectrometer (TOF-MS) [11–14], the determination of T , often referred to as ion thermometry, is less straightforward and various methods have been developed applicable to different

cases. For ions in Coulomb crystals with temperatures $T > 1$ mK, thermometry techniques include the analysis of Doppler-broadened line shapes[15] and dark resonances [16], spatial imaging of single ions and small ion chains [17–19] as well as of large crystals[20–24]. For lower temperatures with ions cooled close to their motional ground state in the trap, resolved-sideband techniques [25–28], applicable mainly to ion chains and small crystals, as well as extensions of this technique [29] applicable to large crystals, have been demonstrated in the past. For higher temperatures, Doppler-recooling [30–33] and time-of-flight experiments [34] have been used.

For Doppler-cooled Coulomb crystals, many of the ion counting and thermometry methods mentioned above rely on interference with the trapped ions, either by destroying the crystals, such as in the time-of-flight method where the ions are ejected from the trap, or potentially changing the ions' attributes, as in Doppler-broadened line-shape analysis where the cooling-laser frequency is scanned and thus the ion temperatures changes. In the image-analysis methods, images of large crystals taken during experiments are compared visually to images generated by molecular dynamics (MD) simulations to infer T and N of the ions[20–24]. In the past, this visual comparison had to be performed *a posteriori* in a time-consuming, iterative simulation procedure and was not implemented in real-time which prevented a rapid and in-situ characterization of the Coulomb crystals during the experiments.

Here, we present a fast, non-perturbative and accurate method to determine these two attributes based on convolutional neural networks (CNNs). In this approach, we first generated a large number of images of crystals of different N s and T s of ions in MD simulations and then trained CNN models on these images to classify these attributes. By comparing the classification results of several popular pre-trained CNN models, we identified the

* yanning.yin@unibas.ch

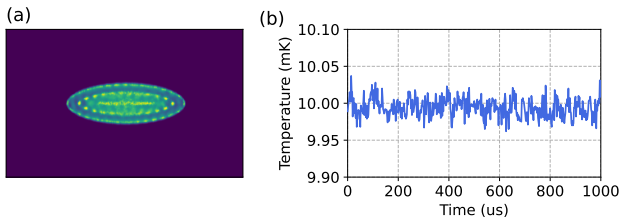


FIG. 1. (a) An example false-color image of a Coulomb crystal with 200 ions and a secular temperature 10 mK. (b) Fluctuation of the temperature after stabilization extracted from the simulation generating the crystal in (a).

best models for determining T and N , respectively. The trained model can be applied to the classification of experimental images and can also be integrated directly into experiments, making real-time and in-situ determination of crystals' characteristics feasible, which offers perspectives to greatly facilitate the analysis and control of trapped ions in experiments.

The paper is structured as follows. Sec. II explains the methods for generating a sufficient number of simulated images for training CNN models, the details of the selection of CNN models as well as the training and validation process. Sec. III provides some examples of applying CNN models to image classification tasks, compares the performances of several CNN models, as well as discusses the implementation of the trained models to classify experimental results. Sec. IV summarizes the main results and suggests potential avenues for further improvements.

II. METHODS

A. Image generation

For training a CNN model, the quality and quantity of images input into the model are crucial for its ultimate performance in terms of accuracy and reliability. Although experimental images of Coulomb crystals taken by cameras would be ideal sources for this task, the collection of such a vast amount of data is painstaking. To our knowledge, to date there is no systematic collection with a sufficient number of images covering a wide range of well-determined values for the salient attributes available. Since image comparison between simulations and experiments is employed routinely as a method for determining N and T , generating a large number of images with varying attributes by simulation was pursued as an efficient way to obtain suitable images for training the CNN model, which was then transferred to the classification of experimental images.

To generate images of Coulomb crystals with a well-defined number and temperature of ions, we adapted the molecular-dynamics (MD) simulation method described

in [35]. Here, the trajectories of N ions inside a RF ion trap were simulated by taking into account the different forces acting on the trapped ions. The force \mathbf{F}_i exerted on an ion i can be written as

$$\mathbf{F}_i = -\nabla U(\mathbf{r}, t) + \mathbf{F}_{\text{Coulomb}} + \mathbf{F}_{\text{cooling}} + \mathbf{F}_{\text{bg}}, \quad (1)$$

where $U(\mathbf{r}, t)$ is the time-dependent trapping potential, $\mathbf{F}_{\text{Coulomb}}$ the Coulomb interaction between ions, $\mathbf{F}_{\text{cooling}}$ the cooling force from photon scattering, and \mathbf{F}_{bg} an effective heating force assumed to be dominated by collisions with background gas.

Generally, the trap potential $U(\mathbf{r}, t)$ is determined by the trap geometry and experimental parameters (DC voltages and RF amplitude/frequency applied to different electrodes). The specific implementation of the trap varies from one experiment to another. In the present work, we used the harmonically approximated potential of a segmented RF trap described in [36],

$$U(\mathbf{r}, t) = \frac{m\omega^2}{8} \sum_i (a_i - 2q_i \cos \Omega t) r_i^2, \quad (2)$$

where m is the mass of the ion, ω the applied RF frequency, r_i the ion position coordinates. Here, Ω was set to $2\pi \times 10$ MHz, and the Mathieu parameters a_i and q_i [8] were derived from numerical modeling: $a_x = -4.62 \times 10^{-4}$, $a_y = -4.10 \times 10^{-4}$, $a_z = 8.83 \times 10^{-4}$, $q_x = 8.73 \times 10^{-2}$, $q_y = -9.15 \times 10^{-2}$, and $q_z = 0$ thus mimicking realistic experimental values.

MD simulations were carried out using the OpenMM framework [37], a high-performance, open-source toolkit supporting both built-in force fields such as Coulomb interactions as well as custom forces and allowing for a speed-up of the computations using graphics processing unit (GPU) acceleration. The cooling force $\mathbf{F}_{\text{cooling}}$ was modeled by momentum kicks of magnitude $\hbar k$ due to photon absorption or emission applied to the ions as they undergo transitions between ground and excited states during laser cooling [35].

While the number of ions N can simply be specified as an input parameter for the MD simulation, the temperature of ions T is less straightforward to control as it depends on the dynamics of the ion ensemble in the presence of several competing interaction terms. One common way to regulate T is to repeatedly apply a velocity kick with a random direction to the ions which represents an overall effective heating effect for various heating processes [22]. However, as examined in [35], adding a velocity kick which essentially resembles an elastic collision of ions with other species (or virtual particles [23]) can cause the ions to sample a broad range of temperatures, especially for infrequent kicks with a large momentum transfer. According to our tests, even adding continuous, weak velocity kicks can cause two severe problems for generating images with a well-defined T . First, the stability of T during the simulation can easily be worse

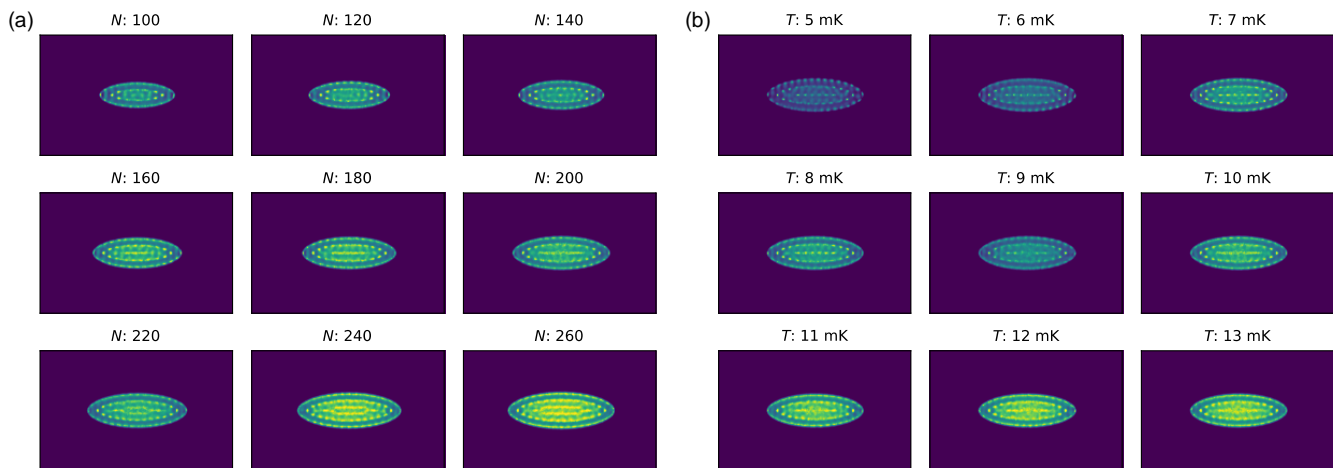


FIG. 2. (a) Example false-color images of Coulomb crystals with different numbers of ions for a fixed secular temperature of $T = 10$ mK. (b) Example images of Coulomb crystals with different secular temperatures for a fixed number of ions $N = 200$.

than ± 1 mK, which would lead to images difficult for the CNN model to classify with an accuracy on that level. Second, there is not a universal velocity-kick frequency and magnitude to generate images with a certain T if their N 's are different, which means a tedious trial-and-error procedure is needed to tune the kick parameters to obtain a desired T once an image with a different N is desired.

To address this issue, we introduced a direct stabilization of T based on feedback control. A target temperature of ions T_{target} was set at the beginning of the simulation. The temperature of the ion ensemble T_{period} was calculated after each RF oscillation by averaging the kinetic energy of N ions according to [22]:

$$T_{\text{period}} = \frac{m}{3Nk_B} \sum_i^N (\bar{v}_{ix}^2 + \bar{v}_{iy}^2 + \bar{v}_{iz}^2) \quad (3)$$

where \bar{v}_{ix} , \bar{v}_{iy} , and \bar{v}_{iz} are the velocity components of the i -th ion averaged over one RF period. In this way, the contribution of the micromotion [8] to the ion velocities was removed from the averaging resulting in a temperature that purely reflects the *secular*, i.e., thermal, motion of the ions in the trap. The difference between T_{period} and T_{target} was then employed as an error signal $e(t)$ to modify the velocities of the ions based on a PID controller. The modified velocity u_i of the i -th ion was related to its previous velocity v_i by

$$u_i^2 = v_i^2 + K_P e(t) + K_I \int e(t) dt + K_D \frac{de(t)}{dt} \quad (4)$$

where K_P , K_I , K_D are the coefficients for the proportional (P), integral (I), and derivative (D) terms in the controller. In practice, we found that only using the P term was sufficient for the stabilization. We then defined

an average of T_{period} over 100 RF periods as the secular temperature of the ion ensemble T .

After T was stabilized, the position of each ion after each time step (1 ns) was recorded and binned into a 3D histogram of positions collected over a duration of 1 ms. From the 3D histogram, 2D slices were extracted along the viewing direction of a camera. For each slice, a Gaussian blur was applied, the intensity of which was varied based on the slice's distance from the central layer to simulate the effect of the finite focal depth of the microscope attached to the camera. All slices were then combined, normalized, and saved as a final simulated image. As an example, Fig. 1 (a) shows an image of a Coulomb crystal with $T=10$ mK and $N=200$ thus generated and Fig.1(b) the corresponding time-dependent temperature after stabilization. It can be seen that the fluctuation of T is within ± 0.04 mK over 1 ms owing to the PID stabilization. This amounts to $\pm 4\%$ relative uncertainty with respect to 1 mK, which is sufficiently precise to serve as training data for a CNN model.

In this way, a large number of simulated images with varying N and T was generated to train the models. As an example, Fig. 2(a) shows a small collection of images of Coulomb crystals generated with different numbers of ions at a secular temperature of 10 mK, and Fig. 2(b) displays crystals with 200 ions at different secular temperatures.

B. CNN models

To classify the images of Coulomb crystals in terms of N and T , we employed one of the most widespread deep-learning methods for image classification, i.e., CNNs[38, 39]. CNNs can automatically and adaptively learn spatial hierarchies of features from input images by applying convolutional and pooling layers, and have proven to be

especially effective in image recognition [39–42].

As a common practice when using CNNs, we adopted transfer learning [43–45] for the present image-classification task. This technique reuses a pre-trained model from other tasks as the starting point for a new task, rather than starting from scratch. During transfer learning, the initial layers of the CNN models can capture generic features while the later layers are fine-tuned to the new task. This approach leverages the knowledge gained from the initial training to accelerate and enhance the new learning process, thus leading to faster convergence and better performance.

Among a large number of pre-trained CNN models that are available for transfer learning, we selected a few widely-used variants, i.e., AlexNet[39], ResNet18[41], Vgg16[40], and MnasNet[42], for our task in consideration of a balance between their performance and computational efficiency. The definitions of these models, including their architectures and the pre-trained weights, are accessible in the *torchvision.models* module of PyTorch [46], an open-source machine learning framework that was utilized in the present work.

C. Training and validation

To use the generated images for training a CNN model, the range of N (or T) to be classified by the model needs to be specified. For example, a given range of $N = 100 - -299$ with a step of 1 will train the model to classify the number of ions in the crystals to differences within one ion count. The specified images are resized to 224×224 pixels as required by the pre-trained CNN models mentioned above. In addition, the original grayscale images can be converted to RGB images. Interestingly, in the present classification it turned out that grayscale images outperformed RGB images for classifying N whereas RGB images gave better accuracy for classifying T . This difference could be explained by noting that for classifying N , shapes and sizes of crystals are more important features in comparison with colors, whereas for classifying T , the additional two color channels of RGB images could offer additional dimensionality for feature extraction, enabling the model to capture more complex patterns across channels.

As we will discuss below, N could be reliably determined by the present models with high accuracy for a much larger number of classes than T . Although it is possible to train a model that can simultaneously classify both N and T , known as multi-label classification, we found that the classification accuracy was significantly lower compared to training models for N or T separately. Therefore, in the remainder of the article, we will focus on the training of individual models.

As an example of classifying $N=100-299$ (in steps of 1 ion), we prepared a total of 7200 images, i.e., 36 images for each class of N , and divided them randomly into training and validation datasets at a ratio of 4:1.

A batch size of 32, chosen based on our GPU capacity, is used for both training and validation. All the CNN models mentioned above can be employed either with or without its pre-trained weights (PTW); the latter means that only the architecture of the model is used. A comparison of classification performances of different models with or without using PTW will be given in the next section, with the help of specific image-classification examples.

After loading the model, its first convolutional layer was modified to accept single-channel input if the images were grayscale, as all the models by default accept three channels for RGB images. Moreover, the last layer of the model was also modified according to the number of classes to be classified. In our example, the last layer was adapted to 200 classes for classifying $N=100-299$ with a step of 1. We used the cross-entropy loss function [39, 47] to measure the dissimilarity between the predicted probability distribution and the true distribution of the target classes, and the Stochastic Gradient Descent (SGD) optimizer with a learning rate of 0.0006 and momentum of 0.9 to update the CNN parameters during the training loop [47].

To accelerate the training and validation process, we employed a GPU (NVIDIA GeForce RTX 2080 Ti) for tensor operations in PyTorch, which could typically reduce the whole training and validation process of 200 epochs to within two hours.

III. RESULTS AND DISCUSSION

A. Image classification examples

For the example of classifying images with $N=100-299$ in steps of 1 ion mentioned above, the training loss and validation accuracy during training are plotted as a function of training epoch in Fig. 3(a), for which the CNN model ResNet18 with its PTW was employed. The training loss refers to the average cross-entropy loss across all batches in the epoch [39, 47], while the validation accuracy refers to the percentage of correctly predicted classes among all predictions made on the validation dataset. During the training loop, the training loss first dropped sharply for the first tens of epochs and then decreased steadily before it stabilized to ≤ 0.001 after about 157 epochs. The validation accuracy shows an opposite trend, increasing from less than 5% to a final stabilized value of 93% after 155 epochs, thus becoming increasingly capable of making correct predictions. It shows clearly that the model’s performance improved significantly during training and could eventually distinguish the validation images with a difference in the number of ions of one ion count with an accuracy better than 90%.

As an example for classifying images of Coulomb crystals with $T = 5-15$ mK in steps of 1 mK, we loaded a total of 2200 images for training, i.e., 200 images are assigned to each class of T . The pre-trained model AlexNet

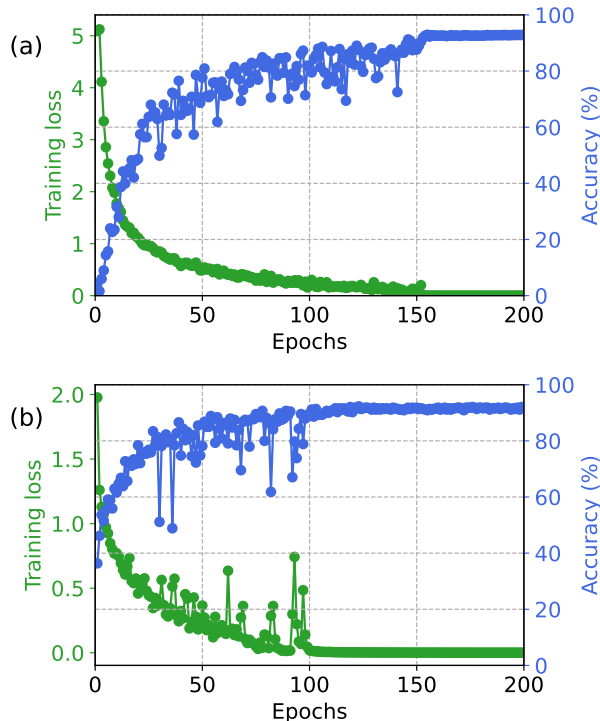


FIG. 3. Training loss (in green) and validation accuracy (in blue) for classifying (a) N in the range of 100–299 ions in steps of 1 ion using the CNN model ResNet18, (b) T in the range of 5–15 mK in steps of 1 mK using AlexNet.

was utilized in this example. Except that the images were converted to RGB, as explained in Sec. II C, the same procedures and hyperparameters (such as batch size, learning rate, number of epochs, etc.) as in the case for classifying N were taken for the training and validation process. The training loss and validation accuracy during training are shown in Fig. 3(b). Both the loss and accuracy converged after ≈ 120 epochs, earlier than the case for N in Fig. 3(a). The final accuracy of 92% highlights the model’s capability of differentiating images with a temperature difference of 1 mK.

To evaluate the distribution of errors, defined as the difference between the model’s predicted class label and the true class label, for the trained models, histograms of errors when applying the models to validation images for the two examples are plotted in Fig. 4. Both histograms indicate a narrow error distribution, with variances of (a) 0.0806 ion counts and (b) 0.0815 mK, respectively. The histogram in Fig. 4(a) is slightly more symmetric than that in Fig. 4. This suggests that there are no systematic biases when applying the model to classify N for the example whereas there is a small bias towards lower temperatures in classifying T , although the errors are centered closely on zero (with means -0.004 and -0.018, respectively).

Note that in the above examples, we let the training loop complete a total of 200 epochs for the sake of illus-

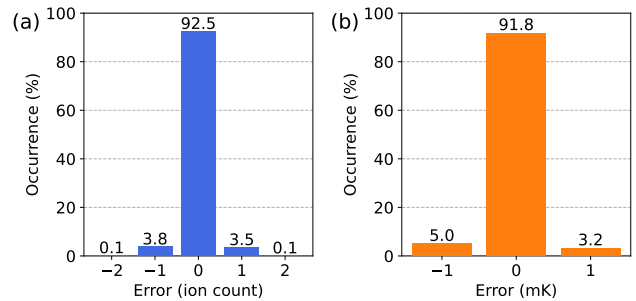


FIG. 4. (a) Histogram of errors when using the trained model ResNet18 to classify 1440 validation images with respect to N in the range of 100–299 ions. (b) Histogram of errors when using the trained model AlexNet to classify 440 validation images with respect to T in the range of 5–15 mK.

tration. However, to avoid possible overfitting after the convergence where the model becomes too specialized in the training data but fails to perform well on new, unseen data [48–51], we terminated the training process earlier in practice when the validation accuracy ceased to improve for 10 consecutive epochs. The model including its architecture and updated weights was saved at the epoch in which the highest accuracy was achieved.

B. CNN model comparison

In the above examples, the classification of N and T over certain ranges was demonstrated using the ResNet18 and AlexNet models, respectively, which proved to give the best performances in comparison with the other CNN models we evaluated. Fig. 5 shows the validation accuracies of all the selected models for classifying N in the range of 100–299 ions in steps of 1 ion and T within 5–15 mK in steps of 1 mK. All models for classifying N (or T) were trained on the same set of images with the same hyperparameters. In this figure, the validation accuracies of models without loading their respective pre-trained weights (PTW) in the training are also depicted. The classification performances generally decrease for both N and T when no PTW was utilized, which confirms the merit of transfer learning. However, the extent to which the accuracies deteriorate vary by model. For example, the use of PTW makes little difference in performance for the model Vgg16, whereas the considerable differences for the model MnasNet1.0 make

TABLE I. Validation accuracies after convergence of different CNN models for classifying T in the range of 5–25 mK (in steps of 2 mK).

Model	AlexNet	ResNet18	MnasNet	Vgg16
Acc.	94%	98%	97%	95%

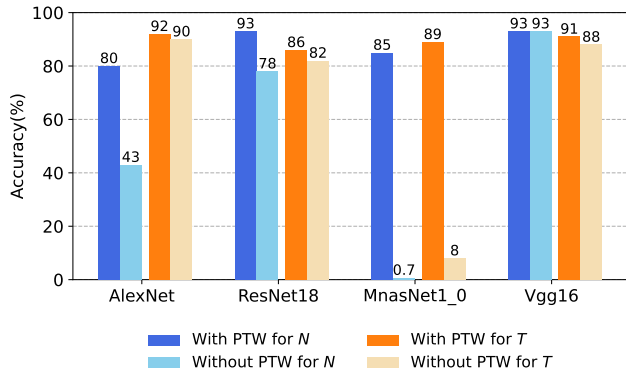


FIG. 5. Validation accuracies after convergence for different CNN models with and without using their corresponding pre-trained weights (PTW) in the training for classifying $N=100$ – 299 ions (step: 1 ion) and for classifying $T=5$ – 15 mK (step: 1 mK)

the use of PTW necessary in this case.

The figure also shows the importance of model selection in order to optimize the classification performance. We see that not only do different models perform quite differently for a specific task (N or T), but the same model can also lead to very different results for different tasks. It also indicates that the model Vgg16 is suitable for both tasks with satisfactory performances.

Note that in our examples, to achieve similarly high validation accuracy (93% and 92% for N and T , respectively), almost six times more images (200 vs. 36) are required for each class for the classification of T with 11 classes than for that of N with 200 classes. Indeed, classifying T appeared to be much more challenging than N . For example, when we increased the range of T to be classified from 5–15 mK (step: 1) to 5–25 mK (step: 1), the validation accuracy after convergence dropped to around 79% with the AlexNet model under the same training conditions. Although $T=5$ – 15 mK is typical temperature range of Coulomb crystals in practical situations [36], we found that a wider range of 5–25 mK could be classified to a high accuracy of 98% with ResNet18 if we could allow the step to be 2 mK, meaning that the model can classify images to temperature differences within 2 mK. For a comparison of classifying $T=5$ – 25 mK (step: 2 mK) with different CNN models, see Table I.

C. Application to the analysis of experimental images

Once a CNN model is trained on the simulated images, the weights of the model with the highest performance saved during training can be used in evaluation mode to classify other images of interest, whether they are from simulations or experiments. While applying the model to simulated images can give a high classification accuracy,

as suggested in Sec. III A, its performance on experimental images may be significantly affected by the quality of the images. Experimental images can differ from simulated ones in terms of noise levels, distortions, contrast, etc., and they are susceptible to changes in experimental conditions. These differences pose challenges to the model’s transferability from simulations to experiments.

In spite of these challenges, we find that a few measures can be taken to alleviate the reduction of the model’s performance when implemented to experiments. Firstly, the parameters used for generating the simulated training images should match or cover the experimental ones. The code used for this paper can easily be adapted to generate simulated images under different experimental parameters on which a new model can be trained. Secondly, when the experiment needs not to discern the variations of temperature or number of ions down to a precision of 1, the model can be trained on images with a higher variation. The classification accuracy should in general increase as the targeted precision is reduced, as can be inferred from Sec. III B. Last but not least, data augmentation [39–41, 52, 53] as an effective method developed in machine learning and computer vision can be employed before the images are fed into training. It is used to increase the size and diversity of training datasets by applying various transformations to the existing images, which can include rotations, scaling, noise injection, etc. It aims to improve the robustness and generalization ability of the machine-learned models, thus enhancing their performance on new, unseen images.

Taking the experimental image shown in Fig. 6(a) as an example, the AlexNet model trained on simulated images to classify T in the range of 5–25 mK in steps of 2 mK predicted a temperature of 5 mK. Meanwhile, the ResNet18 model trained to classify N in the range of 100–299 ions in larger steps of 10 ions predicted 200 ions. The corresponding simulated image with $T = 5$ mK and $N = 200$ ions is shown in Figure 6(b). Noticing that the experiment contains noise in contrast to the simulations, we performed data augmentation by adding Gaussian noise with a mean $\mu = 0$ and a variance $\sigma^2 = 0.1$ grayscale intensity values (which was chosen after testing with a series of variances: 0.01, 0.05, 0.1, 0.15, 0.2, 0.25) to all the simulated images and then retrained the two models. At the cost of a slightly reduced validation accuracy of 86% with AlexNet, the thus obtained model now predicted a temperature of 9 mK for the experimental image. Meanwhile, the retrained ResNet18 model with a validation accuracy of 87% predicted 190 ions for the same image. A direct visual comparison of the corresponding noise-free and noise-augmented simulated images with $T = 9$ mK and $N = 190$ ions shown in Fig. 6(c) and 6(d), respectively, with the experiment in Fig. 6(a) suggests the new predictions to be a more realistic estimate of these attributes compared to the initial guess obtained without adding noise. Two additional examples are given in Fig. 6(e-h), which compares the experimental images with the noise-added simulated im-

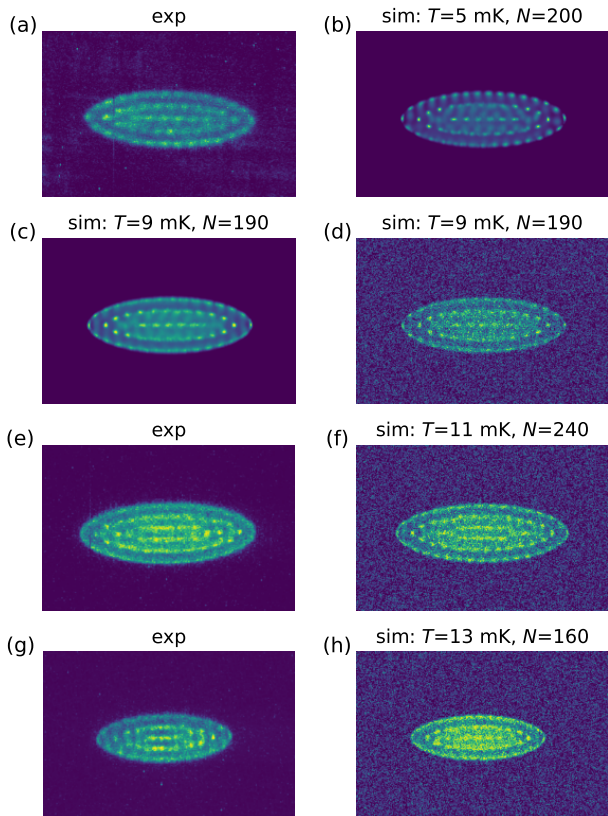


FIG. 6. Comparison between experimental and simulated false-color images with T s and N s predicted by CNN models using the experiment as inputs. (a) First example experimental image. (b) Simulation of (a) with 200 ions at 5 mK. (c) Simulation of (a) with 190 ions at 9 mK. (d) The same simulated image as (c) but with added Gaussian noise. (e) Second example experimental image. (f) Simulation of (e) with 240 ions at 11 mK. (g) Third example experimental image. (h) Simulation of (g) with 160 ions at 13 mK.

ages in which T and N are predicted by the retrained models. By visual comparison of the images, we believe the predicted values provide a fair representation of the experiments.

Apart from applying the model *a posteriori* to pre-recorded experimental images, it can also be directly integrated into an experiment's data acquisition system, allowing an in-situ determination of the relevant Coulomb crystal parameters in real time. According to our evaluation results on a regular lab computer (CPU: Inter Core i7-3930K, RAM: 16 GB, no GPUs), the time for a model to classify an image with 512×512 pixels is a few tens of milliseconds, sufficiently fast to capture changes in crystal characteristics in real time in typical experiments with trapped ions.

IV. CONCLUSION AND OUTLOOK

We demonstrated a fast, accurate, and general methodology for determining the number and secular temperature of ions in Coulomb crystals utilizing convolutional neural networks (CNNs). This methodology involves the generation of a substantial dataset of images depicting crystals with varying parameters, specifically the number of ions and their temperatures, through molecular dynamics simulations. These images serve as training set for CNN models tasked with classifying the aforementioned parameters. Upon evaluating the classification performance of several widely-used pre-trained CNN models, we identified ResNet18 and AlexNet as the most effective for classifying N and T , respectively. Specifically, for crystals with an ion count ranging from 100 to 299 and temperatures between 5 and 15 mK, the best model achieves an accuracy of 93% for the ion count and an accuracy of 92% for the temperature when discerning variations as minute as one ion and 1 mK, respectively.

With a slightly reduced accuracy, the CNN models trained on simulated images can be used for the classification of experimental images. We suggested several ways to improve the performance of experimental implementations, including reducing the classification precision, and pre-processing the simulated input images (e.g. adding noise) before the training. With a direct integration of the model into the experiments, real-time and in-situ determination of crystal parameters can now be feasible, thereby significantly enhancing the monitoring and control of trapped ions in such experiments.

We note that due to the limited number of experimental images with clearly defined ion numbers and temperatures available for model evaluation, the actual performance of the models requires careful verification in real-life experimental settings. Clearly, the quality of the experimental image to be analyzed plays a critical role. Additionally, the manual classification of experimental images by visual comparison with simulated ones which are used to validate the predictions from the models may be subject to inherent inaccuracies. Ideally, the models' predictions would be more reliable if they were trained on a large dataset of experimental images labeled using independent ion counting and thermometry methods, as mentioned in Sec. I. When an insufficient number of experimental images is available, incorporating simulated images into a "hybrid" experimental/ simulated training data set could be beneficial. However, if the models are trained partially or entirely on simulated images, potential systematic errors should be carefully calibrated before applying them to experiments.

The present method is computationally efficient and enables fast data preparation, model training, and evaluation, while also being easily adaptable to different experimental parameters as needed. Furthermore, it can be readily adapted for other ion-trapping experiments, thereby enhancing the ion-counting and thermometry

toolkit for trapped ions in the intermediate temperature range. This compares with other ongoing work of training a general model designed to accommodate a broader range of experimental conditions [54]. Potentially it can also be extended to Coulomb crystals with mixed ions, facilitating studies with sympathetically cooled ions [7, 55] (and the references therein) and dynamics of ion-neutral collisions [7, 56–60].

CODE AVAILABILITY

The code for generating simulated images of Coulomb crystals, training and evaluation of CNN models for ion counting and temperature determination of crys-

tals can be found on the GitHub repository with URL: <https://github.com/yanningyin/Coulomb-crystal-CNN> or on the Zenodo repository with the identifier doi: 10.5281/zenodo.14926184.

ACKNOWLEDGMENTS

We thank Prof. Timothy P. Softley (Birmingham) for helpful discussions. We acknowledge financial support from the Swiss National Science Foundation (Grants nr. 200020_175533, 200021_204123 and TMAG-2_209193) as well as the University of Basel. Y. Y. acknowledges support from the Research Fund of the University of Basel for Excellent Junior Researchers (Grant No. 3CH1051).

-
- [1] C. D. Bruzewicz, J. Chiaverini, R. McConnell, and J. M. Sage, Trapped-ion quantum computing: Progress and challenges, *Appl. Phys. Rev.* **6**, 021314 (2019).
 - [2] C. Monroe and J. Kim, Scaling the ion trap quantum processor, *Science* **339**, 1164 (2013).
 - [3] H. Häffner, C. Roos, and R. Blatt, Quantum computing with trapped ions, *Phys. Rep.* **469**, 155 (2008).
 - [4] D. J. Wineland, Quantum information processing and quantum control with trapped atomic ions, *Phys. Scr.* **2009**, 014007 (2009).
 - [5] A. D. Ludlow, M. M. Boyd, J. Ye, E. Peik, and P. O. Schmidt, Optical atomic clocks, *Rev. Mod. Phys.* **87**, 637 (2015).
 - [6] M. S. Safronova, D. Budker, D. DeMille, D. F. J. Kimball, A. Derevianko, and C. W. Clark, Search for new physics with atoms and molecules, *Rev. Mod. Phys.* **90**, 025008 (2018).
 - [7] S. Willitsch, Coulomb-crystallised molecular ions in traps: methods, applications, prospects, *Int. Rev. Phys. Chem.* **31**, 175 (2012).
 - [8] F. G. Major, V. N. Gheorghe, and G. Werth, *Charged particle traps: physics and techniques of charged particle field confinement*, Vol. 37 (Springer Science & Business Media, 2005).
 - [9] S. Willitsch, M. T. Bell, A. D. Gingell, and T. P. Softley, Chemical applications of laser- and sympathetically-cooled ions in ion traps, *Phys. Chem. Chem. Phys.* **10**, 7200 (2008).
 - [10] F. Schmid, J. Weitenberg, J. Moreno, T. W. Hänsch, T. Udem, and A. Ozawa, Number-resolved detection of dark ions in coulomb crystals, *Phys. Rev. A* **106**, L041101 (2022).
 - [11] C. Schneider, S. J. Schowalter, K. Chen, S. T. Sullivan, and E. R. Hudson, Laser-cooling-assisted mass spectrometry, *Phys. Rev. Appl.* **2**, 034013 (2014).
 - [12] K. A. E. Meyer, L. L. Pollum, L. S. Petralia, A. Tauschinsky, C. J. Rennick, T. P. Softley, and B. R. Heazlewood, Ejection of coulomb crystals from a linear paul ion trap for ion–molecule reaction studies, *J. Phys. Chem. A* **119**, 12449 (2015).
 - [13] P. C. Schmid, J. Greenberg, M. I. Miller, K. Loeffler, and H. J. Lewandowski, An ion trap time-of-flight mass spectrometer with high mass resolution for cold trapped ion experiments, *Rev. Sci. Instrum.* **88**, 123107 (2017).
 - [14] D. Rösch, H. Gao, A. Kilaj, and S. Willitsch, Design and characterization of a linear quadrupole ion trap for high-resolution coulomb-crystal time-of-flight mass spectrometry, *EPJ Tech. Instrum.* **3**, 5 (2016).
 - [15] M. Herrmann, V. Batteiger, S. Knünz, G. Saathoff, T. Udem, and T. W. Hänsch, Frequency metrology on single trapped ions in the weak binding limit: The $3s_{1/2} - 3p_{3/2}$ transition in $^{24}\text{Mg}^+$, *Phys. Rev. Lett.* **102**, 013006 (2009).
 - [16] J. Roßnagel, K. N. Tolazzi, F. Schmidt-Kaler, and K. Singer, Fast thermometry for trapped ions using dark resonances, *New J. Phys.* **17**, 045004 (2015).
 - [17] B. G. Norton, E. W. Streed, M. J. Petrasianus, A. Jechow, and D. Kielpinski, Millikelvin spatial thermometry of trapped ions, *New J. Phys.* **13**, 113022 (2011).
 - [18] S. Knünz, M. Herrmann, V. Batteiger, G. Saathoff, T. W. Hänsch, and T. Udem, Sub-millikelvin spatial thermometry of a single doppler-cooled ion in a paul trap, *Phys. Rev. A* **85**, 023427 (2012).
 - [19] V. Rajagopal, J. P. Marler, M. G. Kokish, and B. C. Odom, Trapped ion chain thermometry and mass spectrometry through imaging, *Eur. J. Mass Spectrom.* **22**, 1 (2016).
 - [20] J. D. Prestage, A. Williams, L. Maleki, M. J. Djomehri, and E. Harabetian, Dynamics of charged particles in a paul radio-frequency quadrupole trap, *Phys. Rev. Lett.* **66**, 2964 (1991).
 - [21] A. Ostendorf, C. B. Zhang, M. A. Wilson, D. Offenber, B. Roth, and S. Schiller, Sympathetic cooling of complex molecular ions to millikelvin temperatures, *Phys. Rev. Lett.* **97**, 243005 (2006).
 - [22] C. B. Zhang, D. Offenber, B. Roth, M. A. Wilson, and S. Schiller, Molecular-dynamics simulations of cold single-species and multispecies ion ensembles in a linear paul trap, *Phys. Rev. A* **76**, 012719 (2007).
 - [23] K. Okada, M. Wada, T. Takayanagi, S. Ohtani, and H. A. Schuessler, Characterization of ion coulomb crystals in a linear paul trap, *Phys. Rev. A* **81**, 013420 (2010).
 - [24] X. Tong, A. H. Winney, and S. Willitsch, Sympathetic cooling of molecular ions in selected rotational and vibrational states produced by threshold photoionization, *Phys. Rev. Lett.* **105**, 143001 (2010).

- [25] J.-S. Chen, K. Wright, N. C. Pisenti, D. Murphy, K. M. Beck, K. Landsman, J. M. Amini, and Y. Nam, Efficient-sideband-cooling protocol for long trapped-ion chains, *Phys. Rev. A* **102**, 043110 (2020).
- [26] L. Feng, W. L. Tan, A. De, A. Menon, A. Chu, G. Pagano, and C. Monroe, Efficient ground-state cooling of large trapped-ion chains with an electromagnetically-induced-transparency tripod scheme, *Phys. Rev. Lett.* **125**, 053001 (2020).
- [27] B. C. Sawyer, J. W. Britton, A. C. Keith, C.-C. J. Wang, J. K. Freericks, H. Uys, M. J. Biercuk, and J. J. Bollinger, Spectroscopy and thermometry of drumhead modes in a mesoscopic trapped-ion crystal using entanglement, *Phys. Rev. Lett.* **108**, 213003 (2012).
- [28] M. D’Onofrio, Y. Xie, A. J. Rasmusson, E. Wolanski, J. Cui, and P. Richerme, Radial two-dimensional ion crystals in a linear paul trap, *Phys. Rev. Lett.* **127**, 020503 (2021).
- [29] I. Vybornyi, L. S. Dreissen, D. Kiesenhofer, H. Hainzer, M. Bock, T. Ollikainen, D. Vadlejš, C. F. Roos, T. E. Mehlstäubler, and K. Hammerer, Sideband thermometry of ion crystals, *PRX Quantum* **4**, 040346 (2023).
- [30] J. H. Wesenberg, R. J. Epstein, D. Leibfried, R. B. Blakestad, J. Britton, J. P. Home, W. M. Itano, J. D. Jost, E. Knill, C. Langer, R. Ozeri, S. Seidelin, and D. J. Wineland, Fluorescence during Doppler cooling of a single trapped atom, *Phys. Rev. A* **76**, 053416 (2007).
- [31] R. J. Epstein, S. Seidelin, D. Leibfried, J. H. Wesenberg, J. J. Bollinger, J. M. Amini, R. B. Blakestad, J. Britton, J. P. Home, W. M. Itano, J. D. Jost, E. Knill, C. Langer, R. Ozeri, N. Shiga, and D. J. Wineland, Simplified motional heating rate measurements of trapped ions, *Phys. Rev. A* **76**, 033411 (2007).
- [32] C. Zipkes, S. Palzer, C. Sias, and M. Köhl, A trapped single ion inside a Bose–Einstein condensate, *Nature* **464**, 388 (2010).
- [33] T. Sikorsky, Z. Meir, N. Akerman, R. Ben-shlomi, and R. Ozeri, Doppler cooling thermometry of a multilevel ion in the presence of micromotion, *Phys. Rev. A* **96**, 012519 (2017).
- [34] M. Nötzold, S. Z. Hassan, J. Tauch, E. Endres, R. Wester, and M. Weidemüller, Thermometry in a multipole ion trap, *Appl. Sci.* **10** (2020).
- [35] I. Rouse and S. Willitsch, Superstatistical velocity distributions of cold trapped ions in molecular-dynamics simulations, *Phys. Rev. A* **92**, 053420 (2015).
- [36] C. Mangeng, Y. Yin, R. Karl, and S. Willitsch, Experimental implementation of laser cooling of trapped ions in strongly inhomogeneous magnetic fields, *Phys. Rev. Res.* **5**, 043180 (2023).
- [37] P. Eastman, J. Swails, J. D. Chodera, R. T. McGibbon, Y. Zhao, K. A. Beauchamp, L.-P. Wang, A. C. Simmonett, M. P. Harrigan, C. D. Stern, R. P. Wiewiora, B. R. Brooks, and V. S. Pande, Openmm 7: Rapid development of high performance algorithms for molecular dynamics, *PLoS Comput. Biol.* **13**, 1 (2017).
- [38] Y. LeCun, Y. Bengio, and G. Hinton, Deep learning, *nature* **521**, 436 (2015).
- [39] A. Krizhevsky, I. Sutskever, and G. E. Hinton, Imagenet classification with deep convolutional neural networks, *Adv. Neural Inf. Process. Syst.* **25** (2012).
- [40] K. Simonyan and A. Zisserman, Very deep convolutional networks for large-scale image recognition, arXiv preprint arXiv:1409.1556 (2014).
- [41] K. He, X. Zhang, S. Ren, and J. Sun, Deep residual learning for image recognition, in *Proc. IEEE Comput. Soc. Conf. Comput. Vis. Pattern Recognit.* (2016) pp. 770–778.
- [42] M. Tan, B. Chen, R. Pang, V. Vasudevan, M. Sandler, A. Howard, and Q. V. Le, Mnasnet: Platform-aware neural architecture search for mobile, in *Proc. IEEE Comput. Soc. Conf. Comput. Vis. Pattern Recognit.* (2019) pp. 2820–2828.
- [43] J. Yosinski, J. Clune, Y. Bengio, and H. Lipson, How transferable are features in deep neural networks?, *Adv. Neural Inf. Process. Syst.* **27** (2014).
- [44] M. Oquab, L. Bottou, I. Laptev, and J. Sivic, Learning and transferring mid-level image representations using convolutional neural networks, in *Proc. IEEE Comput. Soc. Conf. Comput. Vis. Pattern Recognit.* (2014) pp. 1717–1724.
- [45] J. Donahue, Y. Jia, O. Vinyals, J. Hoffman, N. Zhang, E. Tzeng, and T. Darrell, Decaf: A deep convolutional activation feature for generic visual recognition, in *Int. Conf. Mach. Learn.* (PMLR, 2014) pp. 647–655.
- [46] A. Paszke, S. Gross, F. Massa, A. Lerer, J. Bradbury, G. Chanan, T. Killeen, Z. Lin, N. Gimelshein, L. Antiga, *et al.*, Pytorch: An imperative style, high-performance deep learning library, *Adv. Neural Inf. Process. Syst.* **32** (2019).
- [47] I. Goodfellow, Y. Bengio, and A. Courville, *Deep Learning* (MIT Press, 2016) <http://www.deeplearningbook.org>.
- [48] R. Caruana, S. Lawrence, and C. Giles, Overfitting in neural nets: Backpropagation, conjugate gradient, and early stopping, *Adv. Neural Inf. Process. Syst.* **13** (2000).
- [49] L. Prechelt, Early stopping - but when?, in *Neural Networks: Tricks of the Trade*, edited by G. B. Orr and K.-R. Müller (Springer Berlin Heidelberg, Berlin, Heidelberg, 1998) pp. 55–69.
- [50] D. M. Hawkins, The problem of overfitting, *J. Chem. Inf. Comput. Sci.* **44**, 1 (2004), pMID: 14741005.
- [51] Y. Yao, L. Rosasco, and A. Caponnetto, On early stopping in gradient descent learning, *Constr. Approx.* **26**, 289 (2007).
- [52] L. Perez, The effectiveness of data augmentation in image classification using deep learning, arXiv preprint arXiv:1712.04621 (2017).
- [53] C. Shorten and T. M. Khoshgoftaar, A survey on image data augmentation for deep learning, *J. Big Data* **6**, 1 (2019).
- [54] T. P. Softley and J. Allsopp, Coulomb crystals – towards a greater understanding of chemical bonding, in *BEAR PGR Conference Proceedings* (2023) p. 10.
- [55] E. R. Hudson, Sympathetic cooling of molecular ions with ultracold atoms, *EPJ Techn. Instrum.* **3**, 1 (2016).
- [56] M. Tomza, K. Jachymski, R. Gerritsma, A. Negretti, T. Calarco, Z. Idziaszek, and P. S. Julienne, Cold hybrid ion-atom systems, *Rev. Mod. Phys.* **91**, 035001 (2019).
- [57] S. Willitsch, Ion-atom hybrid systems, *Proc. Int. Sch. Phys. Enrico Fermi* **189**, 255 (2015).
- [58] P. Eberle, A. D. Dörfler, C. von Planta, K. Ravi, D. Haas, D. Zhang, S. Y. T. van de Meerakker, and S. Willitsch, Ion-atom and ion-molecule hybrid systems: Ion-neutral chemistry at ultralow energies, *J. Phys.: Conf. Ser.* **635**, 012012 (2015).
- [59] A. D. Dörfler, P. Eberle, D. Koner, M. Tomza, M. Meuwly, and S. Willitsch, Long-range versus short-

- range effects in cold molecular ion-neutral collisions, *Nat. Commun.* **10**, 5429 (2019).
- [60] M. Deiß, S. Willitsch, and J. Hecker Denschlag, Cold trapped molecular ions and hybrid platforms for ions and neutral particles, *Nat. Phys.* **20**, 713–721 (2024).